Surface Science 627 (2014) 75–84

Contents lists available at ScienceDirect

Surface Science

journal homepage: www.elsevier.com/locate/susc

Oxygen chemisorption-induced surface phase transitions on Cu(110)

Qianqian Liu [a], Liang Li [a], Na Cai [a], Wissam A. Saidi [b], Guangwen Zhou [a,*]

[a] Department of Mechanical Engineering & Multidisciplinary Program in Materials Science and Engineering, State University of New York, Binghamton, NY 13902, United States
[b] Department of Chemical and Petroleum Engineering, University of Pittsburgh, Pittsburgh, PA 15261, United States

ARTICLE INFO

Article history:
Received 11 October 2013
Accepted 29 April 2014
Available online 9 May 2014

Keywords:
Oxygen chemisorption
Cu(110)
Scanning tunneling microscopy (STM)
Surface
Reconstruction

ABSTRACT

From an interplay between variable temperature scanning tunneling microscopy and density–functional theory calculations, the evolution of oxygen chemisorption-induced surface reconstructions of the Cu(110) surface is determined. The surface reconstructions proceed via a sequential pathway with increasing oxygen surface coverage. The (2×1) reconstruction occurs first and then transits to the $c(6 \times 2)$ phase with a higher oxygen coverage through a mechanism that consumes the existing (2×1) phase with the supply of Cu adatoms from step edges and terraces. The temperature dependence of the $(2 \times 1) \rightarrow c(6 \times 2)$ transition demonstrates that the surface phase transition is an activated process for breaking up added Cu–O–Cu rows in the (2×1) structure. Comparison between the experimental observations and the theoretical surface phase diagram obtained from first-principles thermodynamic calculations reveals that the $(2 \times 1) \rightarrow c(6 \times 2)$ transition takes place at the oxygen chemical potentials that are far above the chemical potential for Cu_2O bulk oxide formation, reflecting the existence of kinetic limitations to the surface phase transition and the bulk oxide formation.

© 2013 Elsevier B.V. All rights reserved.

1. Introduction

Effects resulting from the interaction between oxygen and a metal surface are of great interest in many areas such as oxidation, corrosion, and heterogeneous catalysis. Acquiring a fundamental understanding of the nature of the interactions is critical to elucidate the role of oxygen for these important technological processes. For instance, many current industrial processes are centered on catalytic oxidation reactions. Upon exposure to an oxygen-containing atmosphere, the metal surface undergoes a series of structural changes varying from the formation of initial oxygen chemisorbed adlayers to oxygen sub-surface diffusion and then to bulk oxide formation, depending on the oxidation conditions including the oxygen gas partial pressure, temperature, and orientation of the metal surface. It has been increasingly apparent that the active phase of some catalytic oxidation catalysts under operating conditions is in fact their oxides rather than the pure metal [1,2]. During catalytic reactions different compositions and structures of the metal surface may be present depending on the operation conditions. However, not all oxide phases are equally active to fulfill multiple catalytic functions. Thus, a detailed study of the formation of each surface reconstruction and the mechanism governing their transitions to other phases will provide insight for finely tuning the operating conditions to favor one phase over the other for better activities and selectivities.

Copper-based catalysts are well known to be active for various catalytic reactions including the water–gas shift reaction [3,4], methanol synthesis and methanol oxidation [5], the reduction and decomposition of nitrogen oxides [6], and fuel cell electrodes [7]. Dissociative adsorption of oxygen, for instance, represents the first step in the synthesis of formaldehyde by methanol oxidation over copper [5]. Surface oxidation and the formation of oxide overlayers are believed to play a critical role in copper catalysis [8,9]. Consequently, Cu has been studied as a prototype system dealing with the oxygen surface chemisorption. Particularly, the oxygen chemisorption on Cu(110), the most open of the low-index surfaces, is among the most studied systems, involving oxygen adsorption, interdiffusion of Cu and O, and various restructuring phases [10–23]. A consensus has been established on some aspects of the behavior of oxygen adsorption on Cu(110) under ultrahigh vacuum (UHV) conditions. Two superstructures occur upon UHV oxygen exposures: an added-row (2×1)–O structure with $\theta = 0.5$ oxygen coverage, and a $c(6 \times 2)$ structure with $\theta = 2/3$ oxygen coverage for increased oxygen exposure [17,19–21].

However, even though the formation of these reconstructed structures has been known for over 20 years, the detailed kinetic and thermodynamic mechanisms controlling the crossover from the added-row (2×1) to the $c(6 \times 2)$ reconstruction are still open for debate. The added-row (2×1) was found to nucleate homogenously on well-ordered terraces and the process can be described as a two-dimensional precipitation of a solid phase from a dilute, mixed fluid of Cu and O [10–23]. Compared to the detailed understanding of the (2×1) reconstruction, very little is known about the formation process of the $c(6 \times 2)$. For instance, it is unclear if the $c(6 \times 2)$ reconstruction can occur directly on an un-reconstructed Cu(110) surface or has to follow a sequential pathway via the $(2 \times 1) \rightarrow c(6 \times 2)$ conversion process when a clean Cu(110) surface is directly exposed to the oxygen

* Corresponding author.
E-mail address: gzhou@binghamton.edu (G. Zhou).

http://dx.doi.org/10.1016/j.susc.2014.04.017
0039-6028/© 2013 Elsevier B.V. All rights reserved.

gas under which the c(6 × 2) reconstruction is thermodynamically more favored over the (2 × 1) reconstruction. Alternatively, if the c(6 × 2) reconstruction occurs by consuming the existing (2 × 1) structure, it will involve massive surface restructuring, the break-up of Cu–O–Cu rows in the (2 × 1) (i.e., a solid–solid transition may be more appropriate), and thus, the effects of kinetic limitations may be equally important in addition to the thermodynamic driving force for the phase transition. Particularly, the requirements of temperature and oxygen pressure delineating the transitions of these surface phases have not been established. Due to the lack of systematic experimental data on the temperature and pressure effects on the surface phase transition, comparisons with theoretical thermodynamic calculations have not been made in the past studies. Our goal in this work is to bridge this information gap by performing a set of experiments with well-controlled temperature and pressure conditions for elucidating the temperature/pressure requirements leading to the crossover from the (2 × 1) to c(6 × 2) reconstructions. Addressing these thermodynamic and kinetic processes governing the surface phase selection is expected to have significant technological implications for controlling the surface structure and reactivity.

In this work we present a systematic study of the effect of oxygen gas exposure and oxidation temperature on the formation of the (2 × 1) and c(6 × 2) phases during the oxidation of Cu(110). Variable temperature scanning tunneling microscopy (STM) is employed to monitor the structure evolution of the surface reconstructions induced by oxygen chemisorption at different temperatures. By examining the oxygen exposure at the oxygen pressure up to 1×10^{-5} Torr at three different temperatures (27 °C, 100 °C, and 350 °C), we demonstrate that the c(6 × 2) formation is temperature dependent, where a critical oxygen coverage is required for the phase transition, thereby supporting the sequential pathway of the surface reconstructions (i.e., the c(6 × 2) reconstruction occurs via the (2 × 1) → c(6 × 2) conversion process). From an interplay between the experiments and the first-principles thermodynamic calculations, we find that a significant kinetic barrier exists for the (2 × 1) → c(6 × 2) phase transition, and toward the bulk oxide formation.

2. Experimental and computational methods

The experiments were performed by an ultrahigh vacuum (UHV) variable-temperature scanning tunneling microscope (Omicron VT-STM XA) with a base pressure of ~1×10^{-11} Torr. An electrochemically etched polycrystalline tungsten wire was used for the STM tip. The STM tips were flashed (1 kV and 2 mA) for several times to evaporate adsorbates and native oxide. Meanwhile, the oxygen dosing was performed in a separate chamber than the STM chamber to ensure the pristine nature of the tip. The Cu(110) single crystal is a 'top-hat' disk (1 mm thick and 8 mm in diameter), purchased from Princeton Scientific Corp., cut to within 0.1° to the (110) crystallographic orientation and polished to a mirror finish. The crystal was cleaned by repeated cycles of Ar^+ sputtering at room temperature (5×10^{-5} Torr of Ar^+, 1 μA cm^{-2}, 1.0 keV) followed by annealing at 600 °C for 10 min. Cleanliness of the Cu(110) surface was checked by STM imaging prior to oxidation by oxygen gas dosing at different temperatures (T = 27 °C, 100 °C, and 350 °C). All the oxidation experiments were carried out on freshly cleaned Cu(110) surfaces. Oxygen gas (purity = 99.9999%) was introduced to the system through a variable-pressure leak valve and the sample was oxidized under a controlled oxygen pressure (pO_2) ranging from 1×10^{-10} Torr to 1×10^{-5} Torr. All the STM images were acquired at room temperature in constant–current mode with bias on the sample.

Density–functional theory (DFT) calculations are performed using the generalized gradient approximation (GGA) of Perdew–Wang (PW91) [24] for the exchange and correlation functional, as implemented in the Vienna Ab-initio Simulation Package (VASP) [25–29]. We used projector augmented wave (PAW) potentials in conjunction with a planewave cutoff energy of 380 eV. The Brillouin-zone integration for the (2 × 1) and c(6 × 2) unit cells is performed using (5 × 7 × 1) and (2 × 4 × 1) Monkhorst–Pack grids [30], and with broadening of the Fermi surface according to Methfessel–Paxton smearing technique [31] with a smearing parameter of 0.2 eV. All of our calculations are spin-averaged except those for the oxygen atom and molecule which are spin polarized. In our modeling of the chemisorbed species on the surface, we used a slab model with five layers where the bottom layer is fixed. Periodic images along the direction perpendicular to the surface are separated by a vacuum region of 12 Å. Adsorption is done on one side of the slab only. Atomic and molecular oxygen are studied using a large cubic cell. The positions of all of the atoms, except those of the bottom layer, are relaxed until the forces are less than 0.015 eV/Å. Various tests have been performed to verify our computational framework such as **k**-grid convergence, vacuum size, and planewave cutoff. As a validity check, our calculated lattice constant for Cu is 3.64 Å which is in good agreement with the experimental value 3.61 Å [32] and with previous calculations [33–35].

We employed a first-principles atomistic thermodynamic framework to assess the relative stability of the considered surface structures as a function of $p(O_2)$ and T [8,13]. The average adsorption energy for single oxygen atom can be defined as,

$$E_O^{ads} = \frac{1}{N_O}\left(E_{O/Cu}^{tot} - E_{Cu}^{slab} - \Delta N_{Cu} E_{Cu} - \frac{N_O}{2} E_{O_2}\right), \quad (1)$$

where $E_{O/Cu}^{tot}$ is the total energy of the Cu–O system, and E_{Cu}^{slab} is the energy of a clean, non-reconstructed Cu surface. ΔN_{Cu} accounts for differences in the number of Cu atoms between the reference clean Cu surface and the Cu–O system, and E_{Cu} is the energy of a single Cu atom in bulk state. E_{O_2} is the energy of an isolated oxygen molecule and N_O is the number of oxygen atoms adsorbed on the Cu substrate. The Gibbs free energy Δγ of the Cu–O system relative to the clean non-reconstructed Cu surface is calculated as,

$$\Delta\gamma = \frac{1}{A}\left[E_{O/Cu}^{tot} - E_{Cu}^{slab} - \Delta N_{Cu}\mu_{Cu} - N_O\mu_O(T,p)\right]. \quad (2)$$

Here A is the surface unit area and μ_{Cu} and μ_O denote the Cu and O chemical potentials, respectively. The chemical potential of Cu is taken to be that of a Cu atom in bulk phase, thus assuming that the slab is in equilibrium with the bulk phase that acts as the Cu reservoir. The oxygen chemical potential depends on temperature and pressure according to

$$\mu_O(T,p) = \frac{1}{2}\left[E_{O_2}^{total} + \tilde{\mu}_{O_2}\left(T,p^0\right) + k_B T \ln\left(\frac{p_{O_2}}{p^0}\right)\right], \quad (3)$$

where p^0 represents the standard atmospheric pressure and $\tilde{\mu}_{O_2}\left(T,p^0\right)$ denotes the chemical potential of oxygen gas at 1 atm, which is tabulated in ref. [36]. In Eqs. (2) and (3), we neglected the vibrational and configurational terms in the Gibbs free energy as these contributions are small [37,38]. Additionally, the −pV contribution is also small for pressures less than 100 atm [38]. By redefining the chemical potential as $\Delta\mu_O = \mu_O - \frac{1}{2}E_{O_2}$ and combining Eqs. (1) and (3), we can express the Gibbs free energies in Eq. (2) as,

$$\Delta\gamma = \frac{1}{A}\left(N_O E_O^{ads} - N_O\Delta\mu_O\right). \quad (4)$$

Before concluding this section, we point out that the GGA/PW91 error for the binding energy for O_2 (the energy that is needed to dissociate an O_2 molecule) is large [35,39,40]. Our calculated value is 6.3 eV while the experimental value is 5.1 eV [41]. Our GGA/PW91 value agrees with previous results [35,39,40]. This error in the binding energy of O_2 affects the thermodynamic analysis. To remedy this, previous studies have used the calculated O_2 binding energy for computing the

phase diagram relying on cancelation of errors when computing energy differences. This is perhaps partially true but oxygen is also a special case and it is not clear whether this is the best approach. In order to estimate a margin of error for our results, we performed our thermodynamic analysis using the computed as well as the experimental binding energy of O_2. In the latter case, we define the "experimentally-corrected" total energy of O_2 as $\frac{1}{2}E_{O_2}^{gas} = E_O^{DFT} - \frac{1}{2}E_{O_2}^{bind}$, where E_O^{DFT} is the DFT energy of an isolated O atom and $E_{O_2}^{bind}$ is the experimental binding energy of O_2. In addition, to ensure that our results are not affected by the choice of exchange–correlation functional, we also use GGA/PBE [40] and LDA [42] formalisms to double check the results. Unless otherwise stated, the theoretical data listed below is obtained using PW91.

3. Results and discussion

The clean Cu(110) surface was oxidized at various temperatures and oxygen pressures ranging from 1×10^{-10} to 1×10^{-5} Torr. All the STM images were obtained on the Cu(110) surface using constant current mode. Fig. 1 shows the STM images of typical large areas and zoomed-in areas of the surfaces oxidized at room temperature (T = 27 °C) under different oxygen pressures and exposure durations. Fig. 1(a) shows the STM images obtained from oxidation at $pO_2 = 1 \times 10^{-10}$ Torr for 5 h of oxygen exposure (i.e., 1.8 L). The surface is covered by alternating wide and narrow stripes. Wide stripes correspond to the bare Cu substrate that results from the relatively low oxygen exposure due to the extremely low oxygen pressure. The narrow stripes are the Cu(110)–(2 × 1)–O reconstructed phase. As revealed by the inset zoomed-in STM image, the (2 × 1) stripes are oriented along the Cu[001] direction. The formation of (2 × 1) stripes on Cu(110) under low oxygen coverage is consistent with previous STM observations [10,18,20,22].

Fig. 1(b) corresponds to the oxidation at $pO_2 = 1 \times 10^{-8}$ Torr for 60 min (oxygen exposure = 36 L). Compared to the reconstruction at the oxygen exposure $pO_2 = 1 \times 10^{-10}$ Torr, the topographic STM images obtained from the surface after the higher oxygen exposure appear quite differently. It can be seen that the step edges become clearly corrugated and the upper and lower terraces exhibit dark depressions that are approximately 1.38 Å deep, which corresponds to single atomic layer deep from the surrounding area [for bulk Cu(110), the single atomic height is 1.27 Å]. As revealed by the inset zoomed-in STM image of Fig. 1(b), the surface is covered by the (2 × 1) phase including in the dark impression areas and tiny areas of the c(6 × 2) phase (the observed c(6 × 2) surface coverage is ~0.012). The formation of the co-existing (2 × 1) and c(6 × 2) phases was also observed in previous STM study [19]. More details for the atomic processes of the (2 × 1) → c(6 × 2) transition are described in Fig. 2.

Fig. 1(c) corresponds to the oxidation at $pO_2 = 1 \times 10^{-6}$ Torr for 40 min (oxygen exposure = 2400 L). Compared to the oxygen exposure at $pO_2 = 1 \times 10^{-8}$ Torr, Fig. 1(c) reveals that the surface becomes roughened with the formation of a high density of one-atomic-deep depressions. The inset zoomed-in STM image shows that the surface is

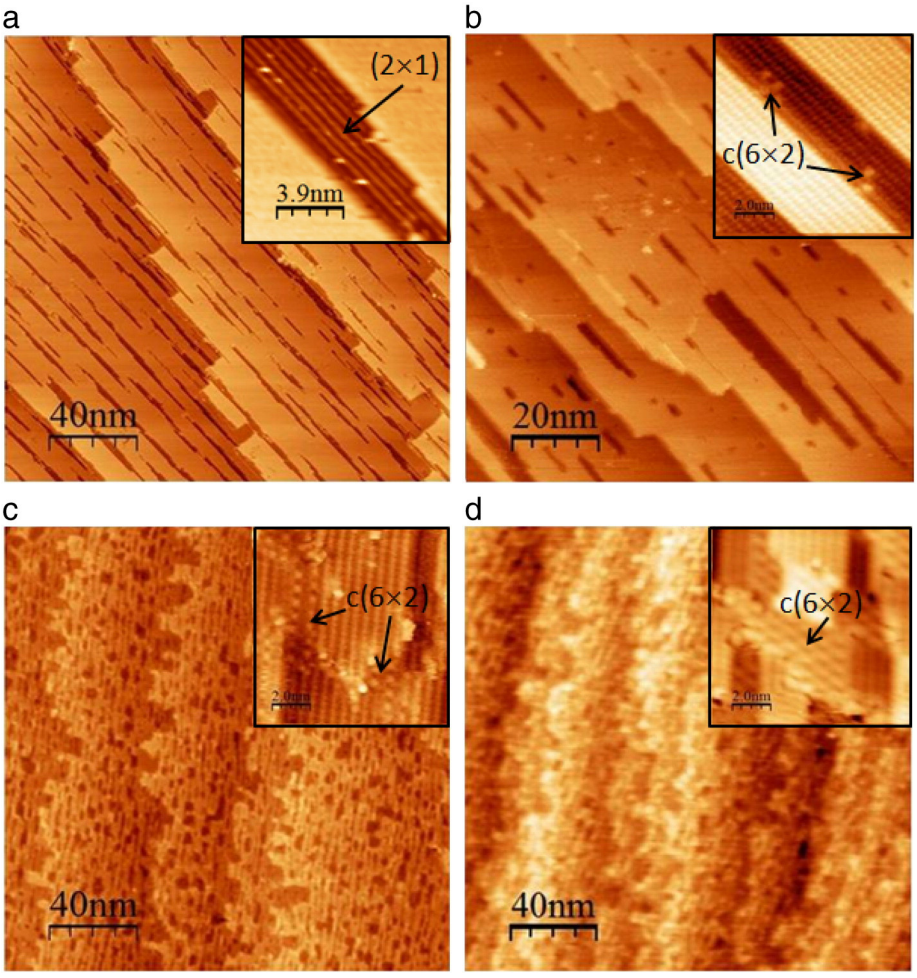

Fig. 1. Topographic STM images of typical large areas of the Cu(110) surface oxidized at room temperature (T = 27 °C) under the different oxygen pressures: (a) $pO_2 = 1 \times 10^{-10}$ Torr for 5 h (exposure = 1.8 L); (b) $pO_2 = 1 \times 10^{-8}$ Torr for 60 min (exposure = 36 L); (c) $pO_2 = 1 \times 10^{-6}$ Torr for 40 min (exposure = 2,400 L); and (d) $pO_2 = 1 \times 10^{-5}$ Torr for 30 min (exposure = 18,000 L). Insets are zoomed-in STM images revealing the atomic structure of the surface reconstructions at the different oxygen pressures. The tunneling conditions for the STM imaging are I_T = 0.1–1 nA and V_B = −2–1.5 V.

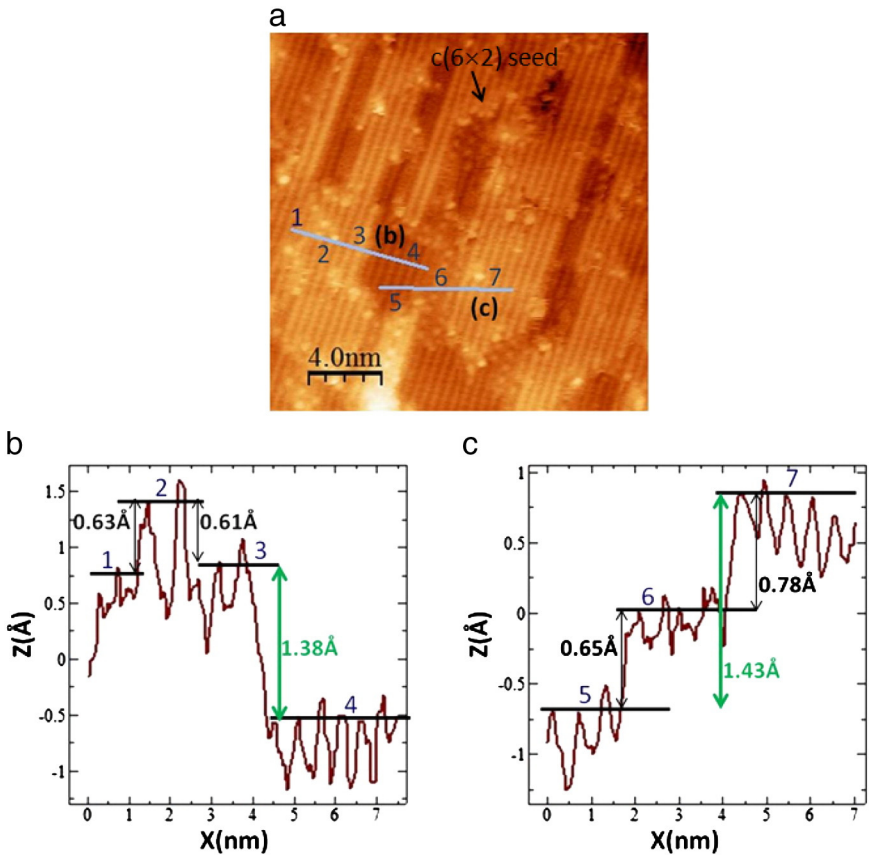

Fig. 2. (a) Representative STM image of the (110) surface oxidized at room temperature (T = 27 °C) under $pO_2 = 1 \times 10^{-6}$ Torr for 40 min revealing the co-existing (2 × 1) and (6 × 2) reconstructions; (b, c) surface profiles along the solid lines marked in (a) reveal the height difference between the different surface regions. The tunneling conditions for the STM imaging are I_T = 0.1–1 nA and $V_B = -2$–1.5 V. (For interpretation of the references to color in the text, the reader is referred to the web version of this article.)

covered by the (2 × 1) phase with tiny islands of the c(6 × 2) phase. Fig. 1(d) corresponds to the oxidation at $pO_2 = 1 \times 10^{-5}$ Torr for 30 min (oxygen exposure = 18,000 L). The topographic STM images indicate that the step edges become highly corrugated and the entire surface is covered with an increased density of depressions compared to Figs. 1(b, c). The inset zoomed-in STM image reveals the coexistence of both (2 × 1) and c(6 × 2) phases, where the coverage of the c(6 ×2) phase is higher compared to the lower oxygen exposures. From the above observations of the Cu(110) surface oxidized under the different oxygen exposures, it becomes clear that the oxygen chemisorption induced surface phase transitions occur via a sequential pathway. The (2 × 1) reconstruction occurs first for the low oxygen coverage and increasing the oxygen surface coverage leads to the (2 × 1) → c(6 × 2) transition. The observations demonstrate that the c(6 × 2) reconstruction does not occur directly on a clean (110) surface despite the significant increase in the oxygen pressure (ranging from $pO_2 = 1 \times 10^{-10}$ Torr to 1×10^{-5} Torr) employed for oxygen exposure. With the increase in oxygen coverage, the c(6 × 2) reconstruction occurs via consuming the existing (2 × 1) phase formed at the low oxygen coverage.

Fig. 2(a) shows a zoomed-in STM image obtained from a terrace of the Cu(110) surface oxidized at room temperature and $pO_2 = 1 \times 10^{-6}$ Torr for 40 min. The topographic STM image reveals that the surface heights become non-uniform due to the formation of depressions. It can be seen clearly that the large two-dimensional domains show the row characteristic of the (2 × 1) phase across the terrace including the depression areas. It is noted that the formation of the c(6 × 2) phase is mostly located in the regions adjacent to the depression areas although some small areas of the c(6 × 2) phase also appear above the adjacent (2 × 1) area, suggesting that the c(6 × 2) phase nucleates on the border of these (2 × 1) depressions as, like step edges, they are source of Cu adatoms. Figs. 2(b, c) display the STM height profile taken along the blue solid lines in Fig. 2(a). Area 2 is a tiny c(6 × 2) island and its surface height is ~0.63 Å above the surrounding (2 × 1) phase (i.e., regions 1 and 3), suggesting that the c(6 × 2) island and its surrounding (2 × 1) phase (i.e., areas 1 and 3) are formed on the same face of the Cu(110) beneath. The height distance between areas 3 and 4 of the (2 × 1) reconstruction is 1.38 Å and between areas 5 and 7 is ~1.43 Å, suggesting that these areas are separated by a single atomic step. Area 6 is a tiny c(6 × 2) region located between areas 5 and 7 and is ~0.78 Å lower than area 7 but ~0.65 Å higher than area 5, implying that the c(6 × 2) island in area 6 is formed on the same plane of the Cu(110) as the neighboring (2 × 1) phase in the depression area (i.e., region 5).

To confirm the height differences of the two phases measured above, we use DFT to calculate the atomic structures of the (2 × 1) and c(6 × 2) phases. Fig. 3 shows the optimized DFT structures of the two oxygenated surface phases. The (2 × 1) structure shows an added row (i.e., Cu–O–Cu chains along the [001] direction) structure with every other [001]Cu atom row absent, and the supercell consists of one Cu–O–Cu chain per two <110>(1 × 1) lattice spacings [20]. The slab comprising 5 atomic layers has a thickness h = 5.16 Å (the slab thickness is defined as the distance between the lowest and highest atom positions along the direction perpendicular to the surface). For the c(6 ×2) structure, the supercell consists of two Cu–O–Cu chains along the [001] direction for each three <110>(1 × 1) lattice spacings and these chains are connected by Cu atoms which are coordinated to every other O atom along the Cu–O–Cu chains [21]. The thickness of the slab of 5 atomic layers in this case is 5.84 Å. Therefore, the c(6 × 2) phase shows up as a protrusion elevated at ~0.68 Å from the adjacent (2 × 1) region if they are formed on the same face of the Cu surface. By comparing the STM height profiles shown in Figs. 2(b, c), the DFT calculated surface

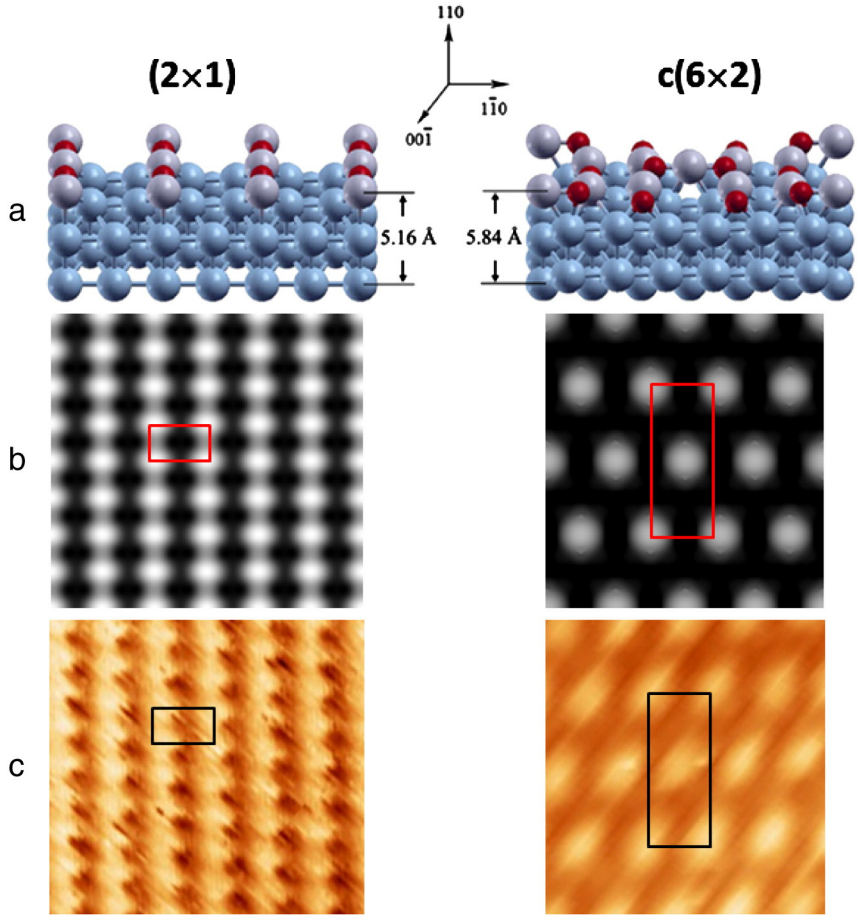

Fig. 3. (a) Atomic structures of the two DFT optimized surface phases of (2 × 1) and c(6 × 2). The surface heights between (2 × 1) and c(6 × 2) differ by ~0.68 Å. (b) Simulated STM micrographs using the structural models of (2 × 1) and c(6 × 2) (shown in a), in which Cu atoms are visible. (c) Experimental STM images of the (2 × 1) and c(6 × 2) reconstructed surfaces. For comparison, the unit cells are delineated in both simulated and experimental images in (b) and (c).

heights of the two phases match well with the experimental data. For instance, the height difference of 1.38 Å between areas 3 and 4 is equal to the single-atomic height step of the pristine Cu(110), while the height difference of ~0.65 Å between the (2 × 1) and c(6 × 2) formed on the same face of the Cu(110) (i.e., areas 5 and 6) agrees well with the DFT result of the surface height difference of the two phases, and the height difference of 0.63 Å between areas 1 and 2 is also very close to the height difference of the (2 × 1) and c(6 × 2) formed on the same Cu(110) face beneath. To provide more evidence, the DFT calculations of the (2 × 1) and c(6 × 2) structural models shown in Fig. 3a are also used to simulate constant–current STM images using the Tersoff–Haman scheme [43] with a bias voltage of −1 V, which is within the range (−2–1.5 V) in the experiments. As can be seen in Figs. 3(b, c), the structural features revealed from the simulated images are similar to the experimental STM micrographs, where Cu atoms are visible in the simulated STM images. By comparing with the simulated and experimental STM images as shown in Figs. 3(b, c), it can be inferred that it is Cu atoms that are observed in the STM images.

It can be seen from Figs. 1 and 2 that the surface terraces become highly corrugated due to the increased oxygen exposure that leads to the c(6 × 2) phase formation by consuming the existing (2 × 1) phase. The growth of the c(6 × 2) domains requires not only the consumption of the existing (2 × 1) region but also the incorporation of new Cu atoms from the substrate, which can be from the terrace or step edges. The origin of such a process can be easily traced to the different surface coverages of Cu and O atoms between the (2 × 1) and c(6 × 2) phases. As shown in Fig. 3, the surface coverages of Cu and O for the (2 × 1) reconstruction are θ = 0.5, which can be translated to an atomic surface density of 0.05/Å^2; while for the c(6 × 2) reconstruction, the surface coverages of Cu and O are θ = 5/6 and 2/3, respectively, which correspond to the atomic surface densities of 0.09/Å^2 and 0.07/Å^2. Apparently, in addition to incorporating Cu and O atoms from the existing (2 × 1) phase, the (2 × 1) → c(6 × 2) transformation requires incorporation of new Cu and O atoms from the surrounding, where O atoms are supplied from the adsorbed oxygen for increased oxygen exposure, while Cu atoms are supplied from the immediate sources of terraces or step edges. It can be noted from Figs. 1(b and c) that the areas of the depressions are much larger than c(6 × 2) islands, suggesting that the initiation of these depressions may be related to the flux of impinging O_2 molecules with respect to the density of Cu adatoms on the terraces and those from step edges. If the oxygen flux is too large (i.e., higher oxygen pressure) while the supply of Cu adatoms from surface steps does not increase correspondingly, the formation of the Cu–O compounds requires another source of Cu atoms, namely the terrace atoms. Then, monolayer depressions can be formed on the terraces. One can see that the depression regions also develop the (2 × 1) reconstruction. When the c(6 × 2) phase appears, it enlarges the depressions with the supply of Cu adatoms from the step edges of these depressions.

It is interesting to note from Fig. 2 that the (2 × 1) reconstruction occurs also for the exposed fresh Cu surface in the depression areas. This further demonstrates that the (2 × 1) phase forms first on a clean Cu(110) surface preceding its transition to the c(6 × 2) phase with increasing the oxygen surface coverage. Since the amount of oxygen coverage on a clean surface builds up gradually upon increasing the oxygen gas exposure and the (2 × 1) reconstruction occurs at the low

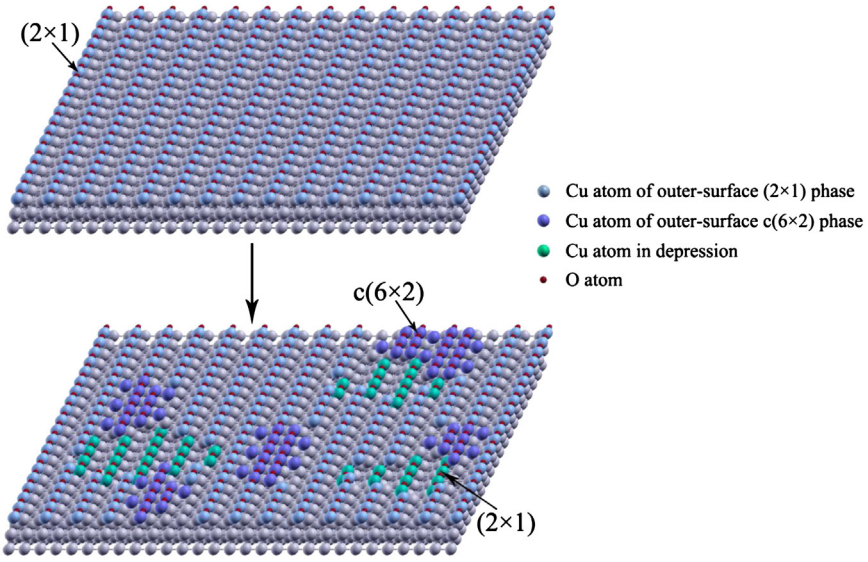

Fig. 4. Pictorial illustration of the $(2 \times 1) \rightarrow c(6 \times 2)$ phase transition. The (2×1) phase forms first on the surface with a saturated oxygen coverage $\theta = 0.5$. Further oxygen uptake leads to the nucleation and growth of $c(6 \times 2)$ islands by consuming the existing (2×1) phase with the supply of Cu adatoms from step edges of the depressions.

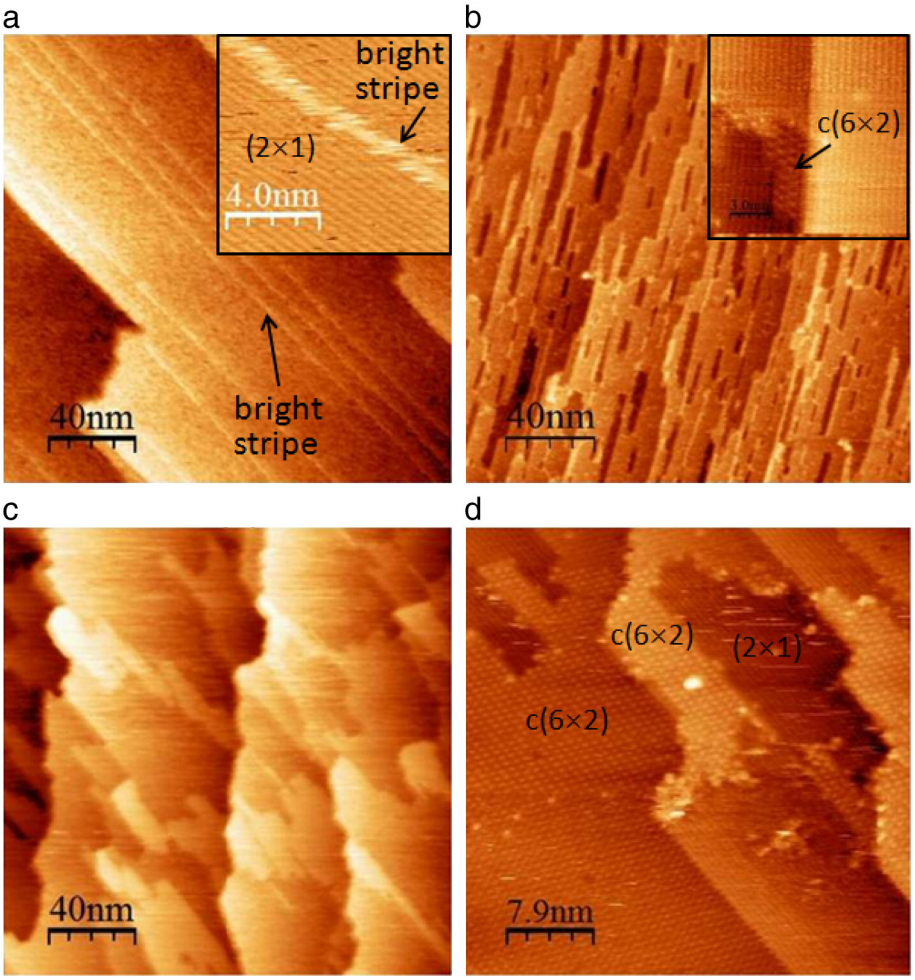

Fig. 5. Topographic STM images of Cu(110) surfaces oxidized at 100 °C: (a) $pO_2 = 1 \times 10^{-8}$ Torr for 60 min (exposure = 36 L); (b) $pO_2 = 1 \times 10^{-5}$ Torr for 4 min (exposure = 2,400 L); and (c, d) $pO_2 = 1 \times 10^{-5}$ Torr for 30 min (exposure = 18,000 L); insets are zoomed-in STM images revealing the atomic structure of the surface reconstructions at the different oxygen pressures. The tunneling conditions for the STM imaging are $I_T = 0.1$–0.6 nA and $V_B = -1.5$–1.5 V.

oxygen coverage, it is clear that the c(6 × 2) reconstruction occurs via a sequential pathway of the (2 × 1) → c(6 × 2) transition despite the magnitude of the oxygen gas pressure examined in our experiments. A pictorial illustration of the (2 × 1) → c(6 × 2) transition described above is given in Fig. 4.

To examine if the surface reconstructions and their phase transitions observed above at room temperature are also temperature dependent, we monitor the surface structures of the Cu(110) oxidized at another two temperatures, one at 100 °C and the other at 350 °C. Fig. 5 illustrates the STM images obtained from the oxidation at T = 100 °C with the different oxygen exposures. Fig. 5(a) corresponds to the oxidation at $pO_2 = 1 \times 10^{-8}$ Torr for 60 min (oxygen exposure = 36 L). It can be seen that surface morphology is smooth including terrace areas and step edges; the step edges are aligned along the Cu[100] direction. Aligned long and bright stripes are also formed on the surface. Zoomed-in STM images as shown in the inset reveal that the entire surface is covered mostly by the (2 × 1) phase co-existing with long bright stripes (the surface coverage of these long bright stripes is ~0.02). The zoomed-in STM image shows that the long-bright stripe is aligned along the (2 × 1)–Cu–O chain direction (i.e., [100]Cu), but the atomic structure of these long bright stripes cannot be resolved clearly from the STM image. By comparing with the oxidation at room temperature under the same oxygen exposure of 36 L, where the (2 × 1) → c(6 × 2) phase transition has also taken place as shown in Fig. 1(b) and the c(6 × 2) phase forms as tiny clusters with a surface coverage of ~0.012, one can see that the same oxygen exposure (36 L) at 100 °C does not show clear sign of c(6 × 2) formation.

Fig. 5(b) illustrates an STM image obtained from the Cu(110) surface oxidized under $pO_2 = 1 \times 10^{-5}$ Torr for 4 min with oxygen exposure = 2400 L. The image reveals that the surface exhibits a large number of depressions across the terraces. Inset zoomed-in STM image shows that the surface is covered by both (2 × 1) and c(6 × 2) phases, where the c(6 × 2) domains have relatively larger sizes than those formed at room temperature under the same oxygen exposure, indicating the enhanced atom mobility at the higher temperature, thus promoting the phase transition. Fig. 5(c) shows the surface oxidized at 100 °C and $pO_2 = 1 \times 10^{-5}$ Torr for 30 min (oxygen exposure = 18,000 L). Rather than forming small depressions as observed from the oxidation at room temperature and the low oxygen exposures, the surface observed here shows large flat areas and narrow stripes across the terraces. Zoomed-in STM images as shown in Fig. 5(d) reveal that the surface is now dominated by the c(6 × 2) phase with small stripes of the (2 × 1) phase, as compared to the much smaller coverage of the c(6 × 2) phase for the same oxygen exposure at room temperature. This growth morphology further demonstrates the enhanced kinetics of the phase transition at the higher temperature. These observations also demonstrate that the (2 × 1) → c(6 × 2) phase transition is driven by the oxygen surface coverage (i.e., thermodynamics aspect), while the kinetic aspect (i.e. temperature effect) of the phase transition becomes dominant once a critical oxygen coverage is reached.

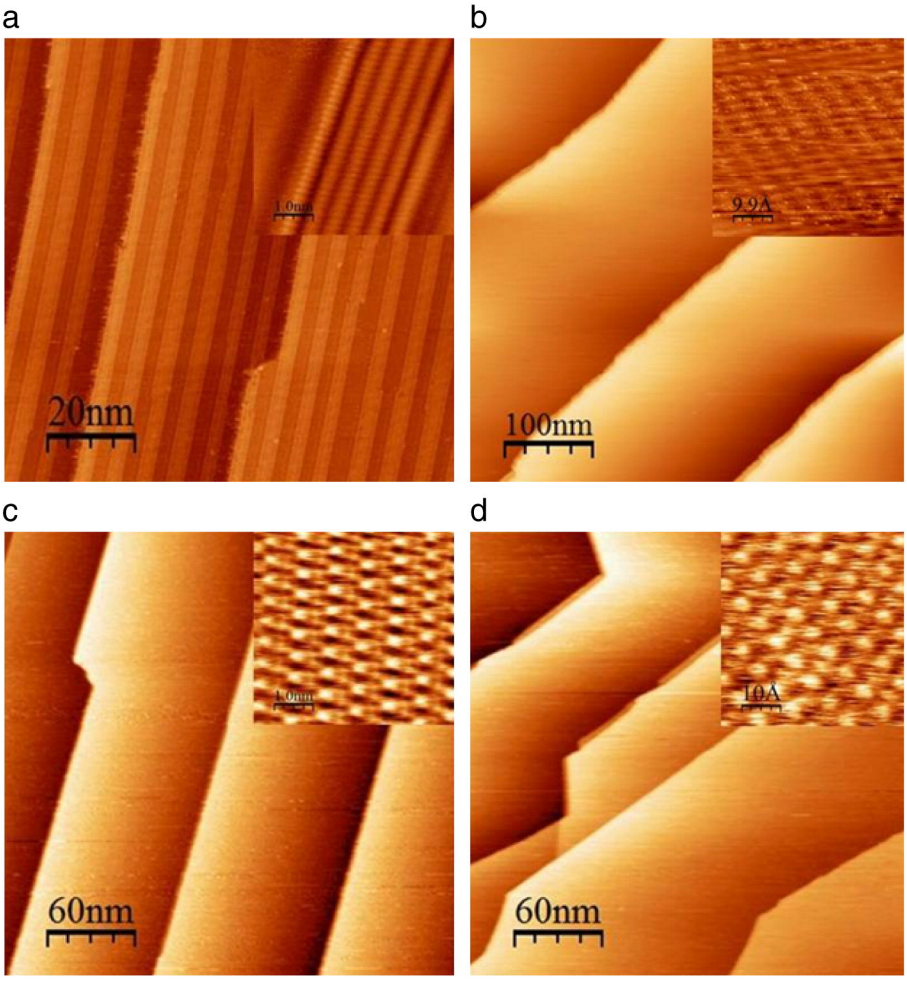

Fig. 6. Topographic STM images of Cu(110) oxidized at 350 °C under the different oxygen gas pressures: (a) $p(O_2) = 5 \times 10^{-9}$ Torr for 10 min (exposure = 3 L); (b) $p(O_2) = 1 \times 10^{-8}$ Torr for 60 min (exposure = 36 L); (c) $p(O_2) = 1 \times 10^{-6}$ Torr for 40 min (exposure = 2,400 L); and (d) $p(O_2) = 5 \times 10^{-5}$ Torr for 40 min (exposure = 120,000 L). Insets are zoomed-in STM images showing the atomic structures of the surface reconstructions at the different oxygen pressures. The tunneling conditions for the STM imaging are I_T = 0.1–3 nA and $V_B = -2$ to −0.3 V.

Fig. 6 shows the oxidation of the Cu(110) surface at 350 °C with the different oxygen exposures. Fig. 6(a) shows an STM image obtained from the surface exposed to $pO_2 = 5 \times 10^{-9}$ Torr for 10 min (exposure = 3 L). Inset is a high-resolution STM image revealing that the surface is only partially covered by well aligned periodic stripes of the (2×1) phase with bare Cu surface, which is similar to the oxidation at room temperature as shown in Fig. 1(a), but having a higher ordered arrangement of the (2×1) stripes due to the enhanced mobility of atoms at the elevated temperature.

Fig. 6(b) corresponds to the oxidation at $pO_2 = 1 \times 10^{-8}$ Torr for 60 min (oxygen exposure = 36 L). It can be seen that the surface morphology is smooth including terrace areas and step edges; the step edges are aligned along the Cu[100] direction. Zoomed-in STM images as shown in the inset reveal that the entire surface is covered by the (2×1) phase. By comparing with the oxidation at room temperature under the same oxygen exposure of 36 L, where the $(2 \times 1) \rightarrow c(6 \times 2)$ phase transition has already started as shown in Fig. 1(b), this oxygen exposure (36 L) at 350 °C still does not reach the oxygen surface coverage required for the formation of the $c(6 \times 2)$ phase. This is also the case for the same amount (36 L) of oxygen exposure at 100 °C as shown in Fig. 5(b). This difference may be attributed to the temperature effect on the effective oxygen surface sticking probability, where the effect from the surface morphology of the Cu(110) surface can be minor since all the oxygen dosing starts with freshly cleaned Cu(110) surfaces with similar surface morphology features (terrace width, step height, etc.). The higher temperature usually leads to a smaller effective oxygen sticking coefficient, and thus a larger oxygen exposure is needed for the phase transition.

Fig. 6(c) shows an STM image of the Cu(110) surface oxidized under a higher oxygen exposure of $pO_2 = 1 \times 10^{-6}$ Torr for 40 min (exposure = 2400 L) at 350 °C. It can be seen that the surfaces in this case have atomically smooth step edges and flat terraces, that is dramatically different from the surfaces oxidized at the lower temperatures with the same amount of oxygen exposure, which are corrugated with high densities of depressions due to the co-existing (2×1) and $c(6 \times 2)$ phases [c.f. Figs. 1(c) and 5(b)]. High-resolution STM images as shown in the inset reveal that the entire surface is fully covered by the $c(6 \times 2)$ phase only. This further supports the earlier observations that the kinetics of the $(2 \times 1) \rightarrow c(6 \times 2)$ transition are greatly enhanced at higher temperature once the critical oxygen coverage is reached for the phase transition. Fig. 6(d) illustrates an STM image obtained from the Cu(110) surface oxidized at 350 °C with the significantly increased oxygen exposure under $pO_2 = 5 \times 10^{-5}$ Torr for 40 min (exposure = 120,000 L), which exhibits similarly atomically smooth step edges and flat terraces as shown in Fig. 6(c). Inset in Fig. 6(d) shows a high-resolution STM image demonstrating that the entire surface is fully covered by the $c(6 \times 2)$ phase only despite the increased oxygen exposure, suggesting that the surface is saturated with the $c(6 \times 2)$ phase and is inert toward further oxidation to form the bulk Cu_2O phase.

The STM observations described above reveal clearly that a critical oxygen surface coverage is required for the $(2 \times 1) \rightarrow c(6 \times 2)$ transition. Increasing the oxidation temperature results in a smaller effective oxygen sticking coefficient and thus a larger oxygen exposure to reach the required oxygen coverage for the phase transition. This demonstrates that the $(2 \times 1) \rightarrow c(6 \times 2)$ transition is driven by the thermodynamics of oxygen coverage. The question arises if the observed surface structures are thermodynamically stable phases under the range of T and pO_2 examined. To identify the microscopic origin of the evolution of the surface structures observed above, we employ a first-principles atomistic thermodynamic framework to assess the relative stability of the (2×1) and $c(6 \times 2)$ structures as a function of pO_2 and T. Using DFT calculations, we computed the oxygen binding energy at the oxygen surface coverage of $\theta = 0.5$ corresponding to the (2×1) structure, and $\theta = 2/3$ corresponding to the $c(6 \times 2)$ structure. The obtained values are −2.12 [−2.72] and −2.00 [−2.59] eV for $\theta = 0.5$ and $\theta = 2/3$, respectively. For each surface reconstruction, we show two values where the first one is calculated using the total computed DFT energy of O_2, while the second value between the parentheses is obtained using the "experimentally-corrected" total energy of O_2. The first set of values obtained with the total DFT energy of O_2 (i.e., −2.12 and −2.0 eV for $\theta = 0.5$ and $\theta = 2/3$, respectively) are in good agreement with the previously reported values of −2.00 and −1.87 eV respectively in ref. [13]. Using Eq. (4), we then calculated the surface free energy for a given T and pO_2 by assuming the full thermodynamic equilibrium of the surface with the oxygen gas. For a given T and pO_2, the preferred surface that we should expect to observe experimentally is the one having the lowest surface free energy under these conditions.

The analysis above leads to the phase stability diagrams. Fig. 7(a) shows the free energies of the considered surface structures plotted against the oxygen chemical potential μ_O. Here we used the experimentally-corrected total energy of O_2 (using the computed DFT energy of O_2 instead would result in a shift of 0.6 eV along the chemical potential horizontal axis of Fig. 7(a)). The upper and lower limits of the oxygen chemical potential for clean Cu(110) surface and the formation of bulk Cu_2O are also determined. In between these two limits, the free energy lines of the more stable reconstructed surface structures intersect one another and their intersection points on the μ axis define the conditions under which a phase changes from one minimum surface free energy to another. The μ scale can be thus divided into several distinct regions in which clean and the two oxygenated surface structures are thermodynamically stable. The phase stability diagram shows a transition of the clean surface into the (2×1) phase at $\Delta\mu_O = -2.12$ [−2.72] eV. As the oxygen chemical potential increases to $\Delta\mu_O = -1.62$ [−2.22] eV, the thermodynamic preference changes from the (2×1) to $c(6 \times 2)$ reconstructions. The $c(6 \times 2)$ reconstruction is the stable phase up to $\Delta\mu_O = -1.46$ [−2.06] eV of the calculated bulk oxide limit, whereas using PBE exchange–correlation functional, this value is determined to be −1.40 [−1.87] eV, and LDA yields −1.60 [−2.98] eV. Fig. 7(b) shows the (pO_2, T) phase diagram with the distinct surface phases obtained by translating the μ boundaries into the temperature and oxygen pressure dependence, where both PW91 and PBE results are shown in solid black curves and dotted blue curves, respectively.

The phase diagram shows the clean Cu surface oxidizes first to the added-row (2×1) phase and then to $c(6 \times 2)$ upon further oxidation, a trend that is in general agreement with experimental results. However, as can be seen from the phase diagram, the (2×1) and $c(6 \times 2)$ phases form at oxygen chemical potentials far above the chemical potential for Cu_2O formation over the whole pO_2 and T regime investigated in our study. Under equilibrium conditions, and for the oxidation at 27 °C, 100 °C and 350 °C, the phase diagram shows that Cu_2O should already form at $pO_2 \sim 1 \times 10^{-57}$, $\sim 7 \times 10^{-44}$, and $\sim 9 \times 10^{-21}$ Torr, respectively. Additionally, for 27 °C, 100 °C and 350 °C, the oxygen gas pressures for the $(2 \times 1) \rightarrow c(6 \times 2)$ phase transition are $pO_2 \sim 5 \times 10^{-63}$, $\sim 4 \times 10^{-48}$, and $\sim 2 \times 10^{-23}$ Torr, respectively. These boundaries in the oxygen pressure are far lower than accessed experimentally. For instance, the experimental value of the oxygen pressure at which we observed the $(2 \times 1) \rightarrow c(6 \times 2)$ phase transition at T = 27 °C for the sufficient oxygen exposure is $pO_2 \sim 1 \times 10^{-8}$ Torr, which is significantly higher than the theoretical oxygen pressure of 5×10^{-63} Torr. Using a gas mixture (e.g. O_2 + Ar) may allow for a much lower oxygen partial pressure in the experiments, but the formation of a (2×1) reconstructed layer under very low oxygen partial pressure would be on a timescale inaccessible by the experiments. However, once the (2×1) reconstruction is formed under a higher oxygen pressure (e.g., 1×10^{-8} Torr), it does not disappear under UHV at a base pressure of 1×10^{-11} Torr in the chamber, suggesting that the rate of oxygen desorption from the surface is very small and the system is far from equilibrium.

The phase diagram obtained using PBE exchange–correlation functional agrees slightly better with the experiments, but the discrepancy is still significant, while LDA phase diagram displays appreciable downward shift compared with that obtained by PW91 functional,

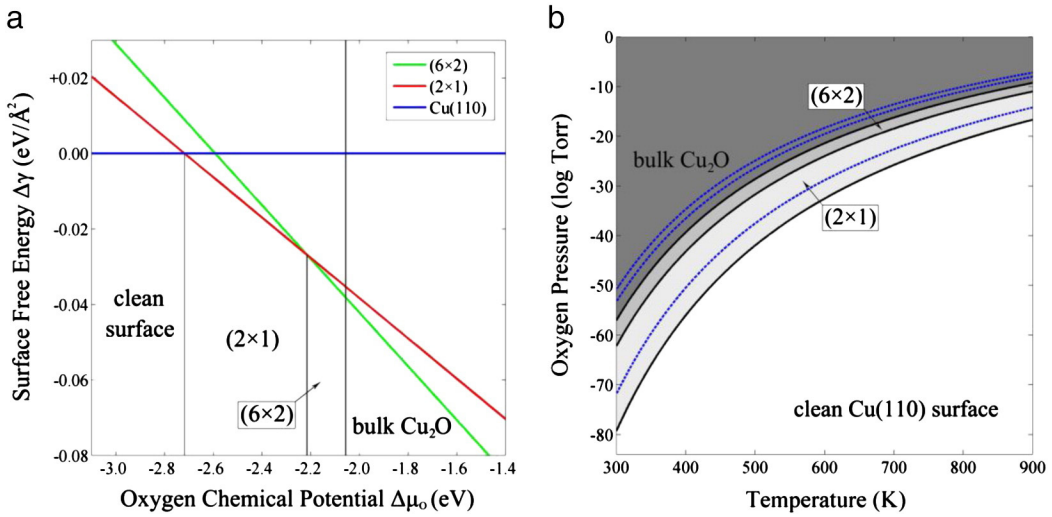

Fig. 7. (a) Surface phase stability diagram for O/Cu(110) system. The surface energy μ of the surface as calculated from DFT is plotted as a function of the oxygen chemical potential μ. (b) (p, T) Phase diagram for the O/Cu(110) systems based on the chemical potential phase boundaries given in (a), where the solid black curves represent the phase boundaries obtained using DFT/PW91 and dotted blue curves obtained using DFT/PBE. (For interpretation of the references to color in this figure legend, the reader is referred to the web version of this article.)

which causes the worst agreement. The difference between the theoretical and experimental values is beyond the margin of error due to the approximations in the ab initio thermodynamics approach or the intrinsic DFT errors, e.g., neglect of vibrational and entropic contributions to free energies, total energy of O_2, as well as uncertainty introduced by the exchange–correlation function. For example, the binding energy of O_2 has to be 8.3 eV in order to get a value for the oxygen pressure that is close to the experimental value; this value is 3 eV higher than the exact binding energy of O_2 and cannot be due to DFT errors. Since the central assumption in our thermodynamic analysis is the full thermodynamic equilibrium of the surface with the environment, we interpret these differences as reflecting the existence of kinetic limitations to the bulk oxide formation. Therefore, the formation of the (2×1) and $c(6 \times 2)$ phases and their transition takes place under metastable conditions of the oxygen chemical potentials that are far above the chemical potential for Cu_2O formation. A clear trend noted from the comparison is that the $c(6 \times 2)$ formation is promoted as the oxidation temperature increases. Such a temperature dependence of the $c(6 \times 2)$ formation suggests a significant activation barrier for this process which can be attributed to the high stability of the Cu–O–Cu chains. This also suggests that one has to go to the high temperature (for instance >400 °C) at which oxygen surface desorption is not negligible for performing experiments addressing thermodynamic equilibrium. In that case, one would need oxygen pressures to stabilize the reconstructions, which may be accessible experimentally.

Clearly, the (2×1) phase represents the thermodynamically most stable structure at the saturated oxygen coverage of $\theta = 0.5$. A larger oxygen coverage drives the $(2 \times 1) \rightarrow c(6 \times 2)$ transition. However, despite the thermodynamic preference of the $c(6 \times 2)$, the incorporation of O and Cu atoms into the $c(6 \times 2)$ structure requires break-up of O–Cu–O added rows of the (2×1) structure and new Cu atoms supplied from the surface beneath. These rows are known to be very stable from their pronounced growth as seen in the (2×1) formation. Therefore, this activation energy has to overcome the breaking up of the O–Cu–O rows in the (2×1) phase. At the low temperature (i.e., 27 °C), the oxidation process is dominated by kinetic limitations, while at higher temperatures thermodynamic properties become increasingly important. Therefore, the observed $(2 \times 1) \rightarrow c(6 \times 2)$ transition as shown in Figs. 1, 5 and 6 reflects the thermodynamic preference of the surface by the $c(6 \times 2)$ phase at the increased oxidation temperature.

The comparison above reveals that the reconstructions occur at the oxygen pressures and temperatures that are far above the thermodynamic equilibrium for Cu_2O bulk oxide formation. This suggests the existence of kinetic barriers to the phase transitions, for instance, due to the energy required to break the existing (2×1) reconstruction to form the $c(6 \times 2)$ phase. Under the oxygen exposure conditions examined in our experiments, the oxygen surface uptake is still far from the saturation, as evidenced by the formation of small $c(6 \times 2)$ islands and (2×1) depressions on the existing (2×1) terraces with increasing the oxygen exposure (shown in Fig. 1). This is also supported by the increased surface coverage of the $c(6 \times 2)$ phase with increasing the substrate temperature and oxygen exposure, suggesting that the oxygen incorporation may be limited by the process of breaking up the existing (2×1) phase, which can be promoted by increasing the substrate temperature. Another possibility of the origin of the kinetic barriers could be related to the dissociation of oxygen molecules on the oxygen chemisorbed Cu(110). Although the energy barrier for the dissociation of O_2 on a nonreconstructed Cu(110) surface is only ~0.1 eV [14,34,44,45], chemisorbed oxygen on the reconstructed Cu(110) may lead to a large energy barrier for the dissociation of impinging oxygen molecules. Under such a situation, the amount of adsorbed oxygen can be practically given by the oxygen that effectively sticks to the surface and not given by a match in the chemical potentials of the oxygen gas and the surface. Some recent in-situ studies (e.g. synchrotron X-ray, which would allow for monitoring equilibrium surface phases if they are present under the real gas conditions) revealed similar kinetic hindrance effect during the oxidation of metallic surfaces such as Pd [46–49]. Our observations from the oxidation of Cu(110) demonstrate the greater universality of the existence of such kinetic hindrance and its effect on the oxygen chemisorbed phase transitions for the range of the temperature examined here, which does not allow for establishing equilibrium between the metal surface and the surrounding gas.

From the temperature dependence of the transformation we conclude that the $(2 \times 1) \rightarrow c(6 \times 2)$ transformation is an activated process. At higher temperatures the supply of Cu atoms is promoted and the mobility within the (2×1) phase is sufficient for a terrace rearrangement, leading to the coexistence of $c(6 \times 2)$ and (2×1) islands under the sufficient thermodynamic driving force (i.e., by increasing the oxygen coverage). The $(2 \times 1) \rightarrow c(6 \times 2)$ transformation can thus be classified as a solid–solid transition in which the break-up of added Cu–O–Cu rows in the (2×1) represents an activated step, which is locally and temporally correlated with the formation of the new phase, as revealed by the formation of the $c(6 \times 2)$ islands mostly adjacent to the depressions on the terraces.

Lastly we discuss the microscopic origin of the formation of the (2×1) and $c(6 \times 2)$ phases under the temperature and pressure conditions

where the formation of Cu_2O bulk oxide is energetically more favorable. Thermodynamically, Cu_2O phase should set in after the $c(6 \times 2)$ phase once the oxygen chemical potential is increased to -1.46 [-2.06] eV. However, the transition from an oxygen chemisorbed phase to the bulk oxide is an activated process involving incorporation of oxygen into the subsurface region [46,50–56], which imposes the high kinetic barriers toward the bulk oxide formation, and therefore a significantly large oxygen gas pressure is needed to nucleate Cu_2O on the surface [57–59]. As a result, the kinetically more favorable processes of surface diffusion of O and Cu atoms lead to the formation of either (2×1) or $c(6 \times 2)$ phase. Such a two-dimensional oxygen-terminated layer can not only further hamper oxygen dissociation but also impede oxygen subsurface diffusion, thereby stabilizing the oxygenated surface under the metastable environmental conditions.

4. Conclusion

The surface reconstructions induced by oxygen chemisorption during the initial oxidation of Cu(110) surface are examined by STM measurements under a wide range of oxygen gas exposures at different temperatures and oxygen pressures varying from 1×10^{-10} to 5×10^{-5} Torr. It is shown that the reaction proceeds in a sequential manner. The (2×1) reconstruction occurs first at the low oxygen coverage with a saturated oxygen coverage of $\theta = 0.5$. Increasing the oxygen coverage beyond $\theta = 0.5$ drives the $(2 \times 1) \rightarrow c(6 \times 2)$ transition. Due to its larger Cu surface coverage, the formation of the $c(6 \times 2)$ requires not only the consumption of the existing (2×1) phase but also the incorporation of underlying Cu atoms that results in the formation of depressions on the surface terraces. Increasing the oxidation temperature leads to a smaller effective oxygen sticking coefficient and thus a larger oxygen exposure needed to reach the critical oxygen surface coverage for the surface phase transition. The temperature dependence of the phase transition demonstrates that the surface phase transition is an activated process associated with breaking up the added Cu–O–Cu rows in the (2×1) reconstruction. The difference between the experimental observations and the theoretical phase diagram obtained from the first-principles thermodynamics calculations reveals that the formation of both (2×1) and $c(6 \times 2)$ phases takes place under metastable conditions of oxygen chemical potentials that favors Cu_2O formation, demonstrating the existence of kinetic limitations to the surface phase transition.

Acknowledgment

This work was supported by the U.S. Department of Energy, Office of Basic Energy Sciences, Division of Materials Sciences and Engineering under award no. DE-FG02-09ER46600. The authors thank N.P. Guisinger for help with the experiments. Use of the Center for Nanoscale Materials was supported by the U.S. Department of Energy, Office of Science, Office of Basic Energy Sciences, under contract no. DE-AC02-06CH11357. This work used the Extreme Science and Engineering Discovery Environment (XSEDE), which is supported by National Science Foundation grant number OCI-1053575.

References

[1] H. Over, Y.D. Kim, A.P. Seitsonen, S. Wendt, E. Lundgren, M. Schmid, P. Varga, A. Morgante, G. Ertl, Science 287 (2000) 1474.
[2] R. Westerstrom, J. Gustafson, A. Resta, A. Mikkelsen, J.N. Andersen, E. Lundgren, N. Seriani, F. Mittendorfer, M. Schmid, J. Klikovits, P. Varga, M.D. Ackermann, J.W.M. Frenken, N. Kasper, A. Stierle, Phys. Rev. B 76 (2007) 155410.
[3] J.A. Rodriguez, P. Liu, J. Hrbek, J. Evans, M. Perez, Angew. Chem. Int. Ed. 46 (2007) 1329.
[4] T. Tabakova, V. Idakiev, J. Papavasiliou, G. Avgouropoulos, T. Loannides, Catal. Commun. 8 (2007) 101.
[5] C. Ammon, A. Bayer, G. Held, B. Richer, L. Schmidt, H. Steinruck, Surf. Sci. 507 (2002) 845.
[6] P.J. Godowski, J. Onsgaard, A. Gagor, M. Kondys, Z.S. Li, Chem. Phys. Lett. 406 (2005) 441.
[7] O. Ilinich, W. Ruettinger, X.S. Liu, R. Farrauto, J. Catal. 247 (2007) 112.
[8] C. Stampfl, Catal. Today 105 (2005) 17.
[9] C. Stampfl, M.V. Ganduglia-Pirovano, K. Reuter, M. Scheffler, Surf. Sci. 500 (2002) 368.
[10] L. Guillemot, K. Bobrov, Phys. Rev. B 83 (2011) 075409.
[11] K. Bobrov, L. Guillemot, Surf. Sci. 604 (2010) 1894.
[12] K. Bobrov, L. Guillemot, Phys. Rev. B 78 (2008) 121408(R).
[13] X. Duan, O. Warschkow, A. Soon, B. Delley, C. Stampfl, Phys. Rev. B 81 (2010) 075430.
[14] L.D. Sun, M. Hohage, R. Denk, P. Zeppenfeld, Phys. Rev. B 76 (2007) 245412.
[15] L.D. Sun, M. Hohage, P. Zeppendfeld, Phys. Rev. B 69 (2004) 045407.
[16] F. Besenbacher, J.K. Norskov, Prog. Surf. Sci. 44 (1993) 5.
[17] F.M. Chua, Y. Kuk, P.J. Silverman, Phys. Rev. Lett. 63 (1989) 386.
[18] K. Kern, H. Niehaus, A. Schatz, P. Zeppendfeld, J. Goerge, G. Comsa, Phys. Rev. Lett. 67 (1991) 855.
[19] D.J. Coulman, J. Wintterlin, J.V. Barth, G. Ertl, Surf. Sci. 240 (1990) 151.
[20] D.J. Coulman, J. Wintterlin, R.J. Behm, G. Ertl, Phys. Rev. Lett. 64 (1990) 1761.
[21] R. Feidenhans, F. Grey, M. Nielsen, F. Besenbacher, F. Jensen, E. Laegsgaard, I. Stensgaard, K.W. Jacobsen, J.K. Norskov, R.L. Johnson, Phys. Rev. Lett. 65 (1990) 2027.
[22] F. Jensen, F. Besenbacher, E. Lasgaard, Phys. Rev. B 41 (1990) 10233.
[23] N. Hartmann, R.J. Madix, Surf. Sci. 488 (2001) 107.
[24] J.P. Perdew, J.A. Chevary, S.H. Vosko, K.A. Jackson, M.R. Pederson, D.J. Singh, C. Fiolhais, Phys. Rev. B 46 (1992) 6671.
[25] G. Kresse, J. Furthmuller, Phys. Rev. B 54 (1996) 11169.
[26] G. Kresse, J. Furthmuller, Comput. Mater. Sci. 6 (1996) 15.
[27] G. Kresse, J. Hafner, Phys. Rev. B 49 (1994) 14251.
[28] G. Kresse, D. Joubert, Phys. Rev. B 59 (1999) 1758.
[29] P.E. Blochl, Phys. Rev. B 50 (1994) 17953.
[30] H.J. Monkhorst, J.D. Pack, Phys. Rev. B 13 (1976) 5188.
[31] M. Methfessel, A.T. Paxton, Phys. Rev. B 40 (1989) 3616.
[32] N.W. Ashcroft, N.D. Mermin, Solid State Physics, Thomson Learning, 1976.
[33] T. Kangas, K. Laasonen, Surf. Sci. 602 (2008) 3239.
[34] M. Alatalo, S. Jaatinen, P. Salo, K. Laasonen, Phys. Rev. B 70 (2004) 245417.
[35] S.Y. Liem, G. Kresse, J.H.R. Clarke, Surf. Sci. 415 (1998) 194.
[36] D.R. Stull, H. Prophet, JANAF Thermochemical Tables, National Standard Reference Data System, 1971.
[37] W.A. Saidi, M.Y. Lee, L. Li, G.W. Zhou, A.J.H. McGaughey, Phys. Rev. B 86 (2012) 245429.
[38] K. Reuter, M. Scheffler, Phys. Rev. B 68 (2003) 045407.
[39] B. Hammer, L.B. Hansen, J.K. Norskov, Phys. Rev. B 59 (1999) 7413.
[40] J.P. Perdew, K. Burke, M. Ernzerhof, Phys. Rev. Lett. 77 (1996) 3865.
[41] C. Herring, in: W.E. Kingston (Ed.), Physics of Powder Metallurgy, McGrall-Hill Books, New York, 1951.
[42] J.P. Perdew, A. Zunger, Phys. Rev. B 23 (1981) 5048.
[43] J. Tersoff, D.R. Hamann, Phys. Rev. B 31 (1985) 805.
[44] J.Y. Ge, J.Q. Dai, Z.H. Zhang, J. Phys. Chem. 100 (1996) 11432.
[45] S.Y. Liem, J.H.R. Clark, G. Kresse, Comput. Mater. Sci. 17 (2000) 133.
[46] E. Lundgren, J. Gustafson, A. Mikkelsen, J.N. Andersen, A. Stierle, H. Dosch, M. Todorova, J. Rogal, K. Reuter, M. Scheffler, Phys. Rev. Lett. 92 (2004) 046101.
[47] A. Vlad, A. Stierle, M. Marsman, G. Kresse, I. Costina, H. Dosch, M. Schmid, P. Varga, Phys. Rev. B 81 (2010) 115402.
[48] R. Westerstrom, C.J. Weststrate, J. Gustafson, A. Mikkelsen, J. Schnadt, J.N. Andersen, E. Lundgren, N. Seriani, F. Mittendorfer, G. Kresse, A. Stierle, Phys. Rev. B 80 (2009) 125431.
[49] R. Westerstrom, C.J. Weststrate, A. Resta, A. Mikkelsen, J. Schnadt, J.N. Andersen, E. Lundgren, M. Schmid, N. Seriani, J. Harl, F. Mittendorfer, G. Kresse, Surf. Sci. 602 (2008) 2440.
[50] G. Ketteler, D.F. Ogletree, H. Bluhm, H.J. Liu, E.L.D. Hebenstreit, M. Salmeron, J. Am. Chem. Soc. 127 (2005) 18269.
[51] R. Blume, H. Niehaus, H. Conrad, A. Bottcher, L. Aballe, L. Gregoratti, A. Barinov, M. Kiskinova, J. Phys. Chem. B 109 (2005) 14052.
[52] P. Dudin, A. Barinov, L. Gregoratti, M. Kriskinova, F. Esch, C. Dri, C. Africh, G. Comelli, J. Phys. Chem. B 109 (2005) 13649.
[53] M. Todorova, W.X. Li, M.V. Ganduglia-Pirovano, C. Stampfl, K. Reuter, M. Scheffler, Phys. Rev. Lett. 89 (2002) 096103.
[54] M.Y. Lee, A.J.H. McGaughey, Surf. Sci. 603 (2009) 3404.
[55] M.Y. Lee, A.J.H. McGaughey, Surf. Sci. 604 (2010) 1425.
[56] Z.H. Gu, P.B. Balburena, J. Phys. Chem. C 111 (2007) 9877.
[57] K. Lahtonen, M. Hirsimaki, M. Lampimaki, M. Valden, J. Chem. Phys. 129 (2008) 124703.
[58] G.W. Zhou, Phys. Rev. B 81 (2010) 195440.
[59] J.A. Eastman, P.H. Fuoss, L.E. Rehn, P.M. Baldo, G.W. Zhou, D.D. Fong, L.J. Thompson, Appl. Phys. Lett. 87 (2005) 051914.